

PROCEEDINGS OF SPIE

SPIDigitalLibrary.org/conference-proceedings-of-spie

Interconnecting wearable devices with nano-biosensing implants through optical wireless communications

Pedram Johari, Honey Pandey, Josep Jornet

Pedram Johari, Honey Pandey, Josep M. Jornet, "Interconnecting wearable devices with nano-biosensing implants through optical wireless communications," Proc. SPIE 10501, Optical Diagnostics and Sensing XVIII: Toward Point-of-Care Diagnostics, 105011C (20 February 2018); doi: 10.1117/12.2288779

SPIE.

Event: SPIE BiOS, 2018, San Francisco, California, United States

Interconnecting Wearable Devices with Nano-biosensing Implants through Optical Wireless Communications

Pedram Johari, Honey Pandey, and Josep M. Jornet

Department of Electrical Engineering
University at Buffalo, The State University of New York
Buffalo, NY 14260, USA

ABSTRACT

Major advancements in the fields of electronics, photonics and wireless communication have enabled the development of compact wearable devices, with applications in diverse domains such as fitness, wellness and medicine. In parallel, nanotechnology is enabling the development of miniature sensors that can detect events at the nanoscale with unprecedented accuracy. On this matter, *in vivo* implantable Surface Plasmon Resonance (SPR) nanosensors have been proposed to analyze circulating biomarkers in body fluids for the early diagnosis of a myriad of diseases, ranging from cardiovascular disorders to different types of cancer. In light of these results, in this paper, an architecture is proposed to bridge the gap between these two apparently disjoint paradigms, namely, the commercial wearable devices and the advanced nano-biosensing technologies. More specifically, this paper thoroughly assesses the feasibility of the wireless optical intercommunications of an SPR-based nanoplasmonic biochip -implanted subcutaneously in the wrist-, with a nanophotonic wearable smart band which is integrated by an array of nano-lasers and photon-detectors for distributed excitation and measurement of the nanoplasmonic biochip. This is done through a link budget analysis which captures the peculiarities of the intra-body optical channel at (sub) cellular level, the strength of the SPR nanosensor reflection, as well as the capabilities of the nanolasers (emission power, spectrum) and the nano photon-detectors (sensitivity and noise equivalent power). The proposed analysis guides the development of practical communication designs between the wearable devices and nano-biosensing implants, which paves the way through early-stage diagnosis of severe diseases.

Keywords: Smart Wearable Band; Implantable Nanoplasmonic Biochip; Nano-biosensing; Noninvasive Optical Diagnosis; Optical Wireless Communications; Intra-body Optical Channel Modeling.

1. INTRODUCTION

In the last decade, major advancements in the field of micro- and nano-electronics, photonics, electro-mechanical systems and wireless communication technologies have enabled the development of compact wearable devices, with applications in diverse fields such as medical, wellness, sport/fitness, security or even business operation. A recent report published by the International Data Corporation (IDC) shows 163.6% increase in wearable device shipments from 28.9 millions units in 2014 to 76.1 million in 2015.¹ In the same report, IDC forecasts that worldwide wearable shipments will reach 173.4 million by 2019. Importantly, among all the wearable devices that have been released so far, the most popular type were medical devices that collect and transmit health-related data.² The interconnection of medical wearable devices in Body Area Networks (BANs)³ is at the basis of innovative healthcare systems. However, despite their potential, existing wearable devices are only able to measure very few parameters, such as heart rate, breathing, temperature or blood pressure.

In parallel to these efforts, nanotechnology is enabling the development of novel nanosensors that are able to detect different types of events at the nanoscale with unprecedented accuracy. Recently, *in-vivo* nanosensing systems, which can operate inside the human body in real time, have been proposed as a way to provide faster

Further author information: (Send correspondence to Pedram Johari)

Pedram Johari: E-mail: pedramjo@buffalo.edu, Telephone: 1 (716) 907-3086

Honey Pandey: E-mail: honeypan@buffalo.edu

Jospe M. Jornet: E-mail: jmjornet@buffalo.edu, Telephone: 1 (716) 645-1607

Optical Diagnostics and Sensing XVIII: Toward Point-of-Care Diagnostics, edited by Gerard L. Coté,
Proc. of SPIE Vol. 10501, 105011C · © 2018 SPIE · CCC code:
1605-7422/18/\$18 · doi: 10.1117/12.2288779

Proc. of SPIE Vol. 10501 105011C-1

and more accurate disease diagnosis and treatment than traditional technologies.⁴ For the time being, researchers have successfully employed surface plasmon resonance (SPR) sensors to analyze circulating biomarkers in body fluids for the diagnosis of deadly diseases, ranging from different cardiovascular and neuronal diseases⁵⁻⁸ to, more recently, different types of cancer directly from blood.⁹⁻¹² However, despite the potential of this technology, there are several limitations in current systems, such as the cost and bulkiness of existing portable systems, which limits the real-world impact of this technology. In addition, one of the main causes of poor survival of cancer patients is the late diagnosis which leads to lack of effective treatment. These reflect the urgent need of next-generation health monitoring and diagnosis systems to overcome the existing challenges and improve the survival of cancer patients.

In light of these results, in this paper, we propose an architecture to bridge the gap between the aforementioned two apparently disjoint paradigms, namely, the commercial wearable devices and the advanced nano-biosensing technologies. This would enable the real-time and early-stage diagnosis of the severe disease, such as cancer, and will eventually lead to more effective treatment plans. More specifically, this paper thoroughly assesses the feasibility of the wireless optical intercommunications of an SPR-based nanoplasmonic biochip -implanted subcutaneously in the user's body (e.g., wrist)-, with a nanophotonic wearable smart band which is integrated by an array of nano-lasers and photon-detectors for distributed excitation and measurement of the nanoplasmonic biochip. This is done through a link budget analysis which captures the peculiarities of the intra-body optical channel, the strength of the SPR nanosensor reflection, as well as the capabilities of the nanolasers (emission power, spectrum)^{13,14} and the nano photon-detectors (sensitivity and noise equivalent power).¹⁵

When designing communication systems to enable the optical wireless connection between the wearable device and the implant, there are two fundamental aspects to take into account. On the one hand, from the communication perspective, the intra-body channel will drastically affect the propagation of optical signals. From the nanoscale perspective, the body is a collection of different types of elements, such as cells, organelles, proteins, and molecules, with different geometry and arrangement as well as different electromagnetic (EM) properties. Despite the challenging propagation of optical signals inside the biological tissues, it is worthy of note that the absorption of water molecules in the optical frequencies is minimal which makes this spectrum range a promising technology for biological applications. Moreover, there have been several recent theoretical^{16,17} as well as experimental^{18,19} studies that prove the fact that certain types of biological cells as well as some synthesized hydrogels behave as optical lenses which can help to increase the propagation distance of optical signals in biological environments. On the other hand, from the biological perspective, the radiation and propagation of optical signals in the body can lead to tissue damage due to photo-thermal effects.²⁰ Moreover, in order to ensure successful chemical binding between the potential biomarkers in the circulatory system and the SPR nanosensor material, the implant has to be placed deep enough to be in touch with sufficient blood vessels. Therefore, a thorough link budget analysis which captures the requirements from both aforementioned perspectives is required, and this is the main focus of the present paper.

The remainder of the paper is organized as follows. In Section 2, a complete system architecture for the multilayer cascade model of the skin tissue and the dielectric properties of different layers is presented. In Section 3, the path-loss and link budget for the optical wireless communication link between the wearable and the implant is studied. Section 4 contains the numerical and simulation results. Finally, we conclude the paper in Section 5.

2. SYSTEM MODEL

Figure 1 depicts the architecture of the a wireless communication link between a wearable device (smart wrist band) and an implanted SPR-based nanoplasmonic biochip in the wrist. The proposed wearable device contains an array of optical nano-sources and detectors for distributed excitation and measurement of the implanted nanoplasmonic biochip. This architecture allows us to move all the active components of the system outside the human body and serves as a nano-to-macro interface between bio-events and the user. The implantable nanoplasmonic biochip consists of nano-patterns for grating-coupled SPR-based detection of the target biomarker. The target biomarker is defined by surface-treating the chip to immobilize selected chemicals.

In this section, we first propose a cascade multilayer approximated model for the different layers of the human skin. This multilayer model enables more tractable calculation of the path-loss and link budget analysis. Then,

we focus on the light/matter interaction and the wave propagation analysis for the communication link between the wearable device and implanted biochip based on the proposed multilayer structure.

2.1 Cascaded Multilayer Skin Tissue Model

The human skin is in fact made of tissues that work together as a single structure to perform unique and critical functions. The skin and its accessory structures make up the integumentary system, which provides the body with overall protection. The skin is made of multiple layers of cells and tissues, which are held to underlying structures by connective tissue (Figure 1). The deeper layer of skin is well vascularized (has numerous blood vessels), while, the uppermost layer of the skin, i.e., epidermis does not contain any blood vessel. In order to obtain accurate disease diagnosis data, we need to guarantee successful chemical binding between the potential biomarkers in the circulatory system and the SPR nanosensor material. Therefore, on the one hand, the implant has to be placed deep enough to be in touch with sufficient blood vessels and fulfill minimum blood/implant interactions. However, on the other hand, the scattering and absorption losses of the EM radiation through skin layers in the near-infrared region (780–2500 nm) is very high which restricts the achievable penetration depth within the range of 1–6 mm.²¹ In view of these results, an optimal depth for the implant has to be found in order to satisfy the requirements from both the biological and communication perspectives.

In our analysis, we utilize a multilayer cascade model²² for the skin tissue to study the path-loss and link budget analysis. More specifically, to simplify and approximate the complicated human skin tissue structure, we consider the path between the wearable and implant as a cascade layered structure of different cell types. As depicted in the right hand side of Figure 1, we consider four different layers, namely, air, skin (epidermis and dermis layers), blood, and fat. In this figure, “Th” refers to the thickness of each layer. Moreover, as shown in the figure, we consider fixed thickness for all layers except for the fat where the implant is considered to be placed somewhere in this layer. The thickness of the fat layer is further defined as a parameter in our analysis which is related to the depth of the implant which has to be chosen depending on the required level of blood vessels in contact with the SPR nanosensor. Furthermore, we consider the implant to be made from gold based on the wide applications of gold material for the SPR sensors on detection of chemical and biological species.^{23,24}

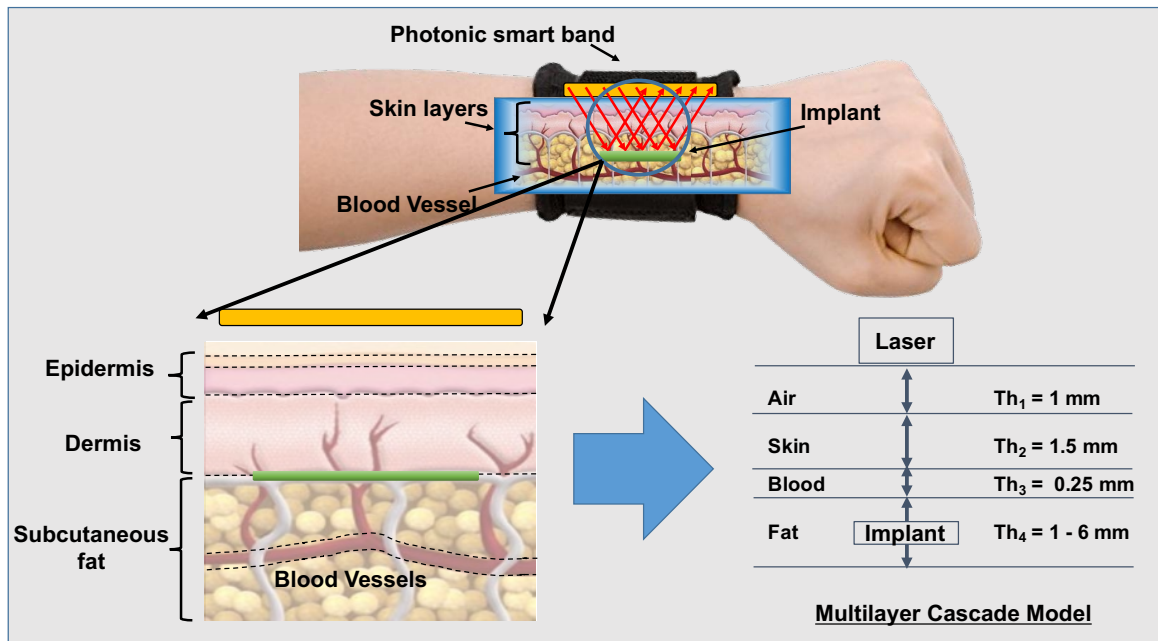


Figure 1: (a) Multilayer cascade model of skin tissue for wearable to implant communication channel modeling.

2.2 Light/Matter Interactions with Human Skin Tissue

When the light propagates in the biological tissues, there are four main phenomena that might occur as follows:

- *Absorption*, where the light energy is absorbed and converted to heat as the result of atoms and molecule vibration. The atoms and molecules have the selective natural behavior of certain light frequency absorption. The absorption of a certain material is typically defined by a parameter called *absorption coefficient*, μ_{abs} which depends on the wavelength of the EM wave.
- *Scattering*, which can be perceived as deflection of the ray of light from a straight path due to heterogeneous medium or the interface between two media. As the light experiences scattering, it might be deviated in different angles (omni direction, forward, or backward scattered) based on the size of the particles compared to the wavelength of the incident light. Light scattering in biological tissues is well defined by the *Henye-Greenstein* phase function introducing the coefficient *anisotropy factor*, g . For biological tissues, typically this parameter is in the range of $0.5 \leq g \leq 0.95$, which indicates that forward scattering is dominant. For a more accurate model of light propagation in biological tissues, the reduced scattering parameter, $\mu'_s = (1 - g)\mu_s$, is used since the light undergoes multiple scattering effect.²⁵
- *Reflection*, is the phenomenon where the direction of the light propagation is reflected back to the same medium as it is originated. For biological tissues, diffuse reflection is most likely to occur. The common simplification for biological environment is by assuming that the surface is *Lambertian*.²⁶ However, for smooth and large particle in comparison to the wavelength and in the case of very small illumination areas, the specular reflection is valid and can be considered as a good approximation.
- *Refraction*, occurs due to the light traversing via two media with different density. This causes the change in propagation direction. This phenomenon is described by *Snell's law* where ratio of the angle of incident θ_i and refraction θ_r is proportional to the phase velocities (v_1/v_2), or equivalently, inversely proportional to refraction indices of the two media (n_2/n_1):

$$\frac{\sin\theta_i}{\sin\theta_r} = \frac{v_i}{v_r} = \frac{n_r}{n_i}. \quad (1)$$

It is relevant to note that, the *refractive index* of a material is related to its dielectric properties through the equation $n(w) = \sqrt{\mu_r(w)\epsilon_r(w)}$ which depends on the wavelength or equivalently on the frequency of the EM radiation. Since the biological tissues are non-magnetic at the optical frequencies, the value of the *relative permeability*, μ_r , is considered to be equal to one, i.e., the biological materials are not responsive to magnetic fields. Therefore the real and imaginary parts of the *refractive index* and the *relative permittivity* are related to each other as follows:

$$\epsilon_r = n(w)^2 = n_r(w)^2 - n_i(w)^2 - j2n_r(w)n_i(w) \quad (2)$$

where, ϵ_r is the complex number of *relative permittivity*, and $n(w) = n_r(w) - jn_i(w)$ is the *refractive index* of the material at the frequency $w = 2\pi f$ or equivalently wavelength λ . The real part, $n_r(w)$, accounts for the refraction and is usually measured directly, where as the imaginary part, $n_i(w)$, deals with absorption and can be obtained from the *absorption coefficient*, μ_{abs} , as follows:

$$n_i(w) = \mu_{abs}\lambda_g/4\pi \quad (3)$$

Table 1 summarizes all the parameters of different layers of the our multilayer structure at the wavelength of 1500 nm. The **bold-face** numbers in the table are collected from the literature (cited in the table for different materials), and the *italic-face* numbers are derived from the given properties by using the equation (3).

Table 1: Dielectric and refractive properties of different materials at $\lambda = 1500$ nm.

	Real Part of Refractive Index	Imaginary Part of Refractive Index	Thickness	Relative Permittivity	Absorption Coefficient	Reduced Scattering Coefficient
Material	$n_r(w)$	$n_i(w)$	$t(mm)$	ϵ_r	$\mu_{abs}(mm^{-1})$	$\mu_{sca}(mm^{-1})$
Air ²⁷	1	0	1	1	0	0
Skin ²¹	1.41	$1.79e-5$	1.5	$1.87-j4.58e-4$	1.50e-1	1.47
Blood ^{28,29}	1.35	$3.58e-4$	0.25	$1.82-j9.67e-4$	2.99	5.2e-1
Fat ²¹	1.46	$1.35e-5$	1-5	$2.13-j3.94e-5$	1.13e-1	7.27e-1
Implant ³⁰	0.49	10.353	0.5	$-106.94-j10.14$	$8.67e+4$	–

3. PATH-LOSS AND LINK BUDGET ANALYSES

In a communication system design, link budget analysis is the essential starting point for estimating the different losses encountered as the signal propagates from the transmitter to the receiver. A comprehensive and accurate model that predicts all the losses within the communication link is important for predicting the required transmitter power as well as the required receiver sensitivity. Link budget analysis for the intra-body communications has been studied in both Terahertz and Optical frequencies.^{22,31} However, the round-trip link budget in the proposed multilayer cascade model (signal being transmitted from the wearable device, reached to the implant and being reflected, and finally received back in the wearable device) for interconnecting the wearable and implants has not been investigated in the literature. In order to perform link budget analysis for the model in Figure 1, the gains and losses for the path from the transmitter, through the medium (in this case the human skin tissue) to the implant and back to the receiver must be taken into account. In general, the link budget equation is given as:

$$P_R(dBm) = P_T(dBm) + G_T(dB) - Losses(dB) + G_R(dB) \quad (4)$$

where P_R and P_T are the received and transmitted powers, and G_T and G_R are the gains of the transmitting and receiving antennas, respectively. *Losses* include all the attenuations with respect to the wave propagation through different layers of the skin tissue as well as at the boundaries between the two layers that will be further investigated in the following subsections.

The path loss is contributed by three frequency dependent factors, namely, the spreading loss L_{spr} , the molecular absorption loss L_{abs} and the scattering loss L_{sca} . Every term represents the input to output ratio of the EM field intensity after traveling through a particular distance in a specific medium. The total path loss in dB is given by

$$L_{Path} = L_{spr} + L_{abs} + L_{sca}. \quad (5)$$

- *Spreading Attenuation:* The spherical spreading of energy causes loss in the EM waves which is quantitatively described by the following equation:

$$L_{spr} = 10 \log_{10} \left(\frac{1}{D} \left(\frac{4\pi}{\lambda_g^2} \right) (4\pi d^2) \right), \quad (6)$$

where λ_g is the effective wavelength, λ/n , (n is the real part of refractive index of the medium), and d is the distance from the radiation source. This equation has three terms, namely, $(4\pi/\lambda_g^2)$ which is the antenna effective aperture; $4\pi d^2$ which is the spherical spreading loss; and the antenna directivity gain, D , which is defined as the ratio of the solid angle of a sphere to the radiation solid angle of the antenna, Ω_A as follows:

$$D = 4\pi/\Omega_A. \quad (7)$$

This radiation solid angle depends on the specific radiation pattern of the antenna. For a narrow directional source with narrow beam width $\Delta\theta$ and $\Delta\phi$, Ω_A is given as

$$\Omega_A = \int_{\phi=0}^{\Delta\phi} \int_{\theta=0}^{\Delta\theta} \sin\theta d\theta d\phi = \Delta\phi(1 - \cos\Delta\theta), \quad (8)$$

where θ and ϕ are the azimuth and polar angles in the spherical coordinate system, respectively.

- *Absorption and Scattering Attenuations:* The skin tissue is composed of nanoscale bio-molecular structures that absorb and scatter the light intensity and eventually affect the propagation of the EM wave radiation. The total attenuation due the molecular absorption and scattering is given by:

$$L_{as} = e^{(\mu_{abs} + \mu_{sca})d}, \quad (9)$$

where d is the distance that the wave traverse, μ_{abs} and μ_{sca} are the absorption and reduced scattering coefficients of the media respectively, which have been explained earlier in Table 1, Section 2.2.

In addition to the loss due the aforementioned phenomena, we need to consider the boundary loss L_{bound} which is the attenuation of the EM source intensity when traversing across the boundary of two media. Fresnel's equations explain the attenuation of refracted ray as the light travels from one medium to another having different refractive indices. According to the Fresnel's law, when the light is propagating from one medium to another, part of the light is reflected and part of it is refracted at the boundary and travels in the secondary medium with a different angle accordingly. This behavior depends on the polarization of the incident ray which can be composed of both s-polarized and p-polarized waves. In our analysis, we consider the ray of incidence is normal to the plane and hence the s-/p-polarized refraction equations are the same. This requires very directive radiation pattern of the transmitted wave which is achievable with the state-of-the-art micro-ring lasers.¹³ We define R and T as the reflectance and transmittance of the lights respectively, which can be obtained as:

$$R = (|(n_1 - n_2)/(n_1 + n_2)|)^2, \quad (10)$$

$$T = 1 - R. \quad (11)$$

Therefore, the boundary attenuation L_{bound} is given by the following equation

$$L_{bound} = 10 \log_{10}(T). \quad (12)$$

Moreover, at each boundary, there will be a portion of light which will be reflected back and the attenuation caused by the reflection can be given as $L_{ref} = 10 \log_{10}(R)$.

4. SIMULATION RESULTS AND NUMERICAL ANALYSIS

4.1 Multiphysics Simulation Results for the Boundary Transition Losses

It is worthy of note that performing the simulation for the entire model in Figure 1 including the path-loss in frequency domain and time delays for the reflected signals in the time domain are not feasible in a timely manner due to the very large size of the medium (in the range of millimeters) compared to our wavelength (1500 nm). However, the transition boundary losses between two media can be simulated by zooming into a very small area close to the interface of the adjacent layers. Therefore, to further validate our analysis, Figure 2 shows the light penetration/reflection pattern in the boundaries between two different layers in our cascade multilayer model using a point dipole antenna as the transmitting source. COMSOL Multiphysics³² has been used to perform the simulations by solving the Maxwell EM equations in the frequency domain. In Figure 2 (a)-(d), the propagation pattern of the EM wave is shown, and in Figure 3 the path-loss over a cut-line that passes through the antenna and the center of the media (perpendicular to the boundary) is shown for the transition boundary of air to skin. It can be observed from Figure 3 that largest loss happens in the boundary of air and skin, i.e., when the light propagates into the first layer of the skin tissue. This is due the large difference between the refractive indices of air and skin. The fluctuation in the wave intensity in Figure 3 right before the transition boundary shows the reflected signal at the air-skin interface. In contrast, as it can be observed from Figure 2, the penetration loss is much smaller and almost negligible in the boundary of skin and blood as well as the blood and fat layers. Finally, at the implant, most of the light will be reflected back which is due to the high reflectivity of gold as will be explained later in the numerical analysis results (Figure 4 in Section 4.2).

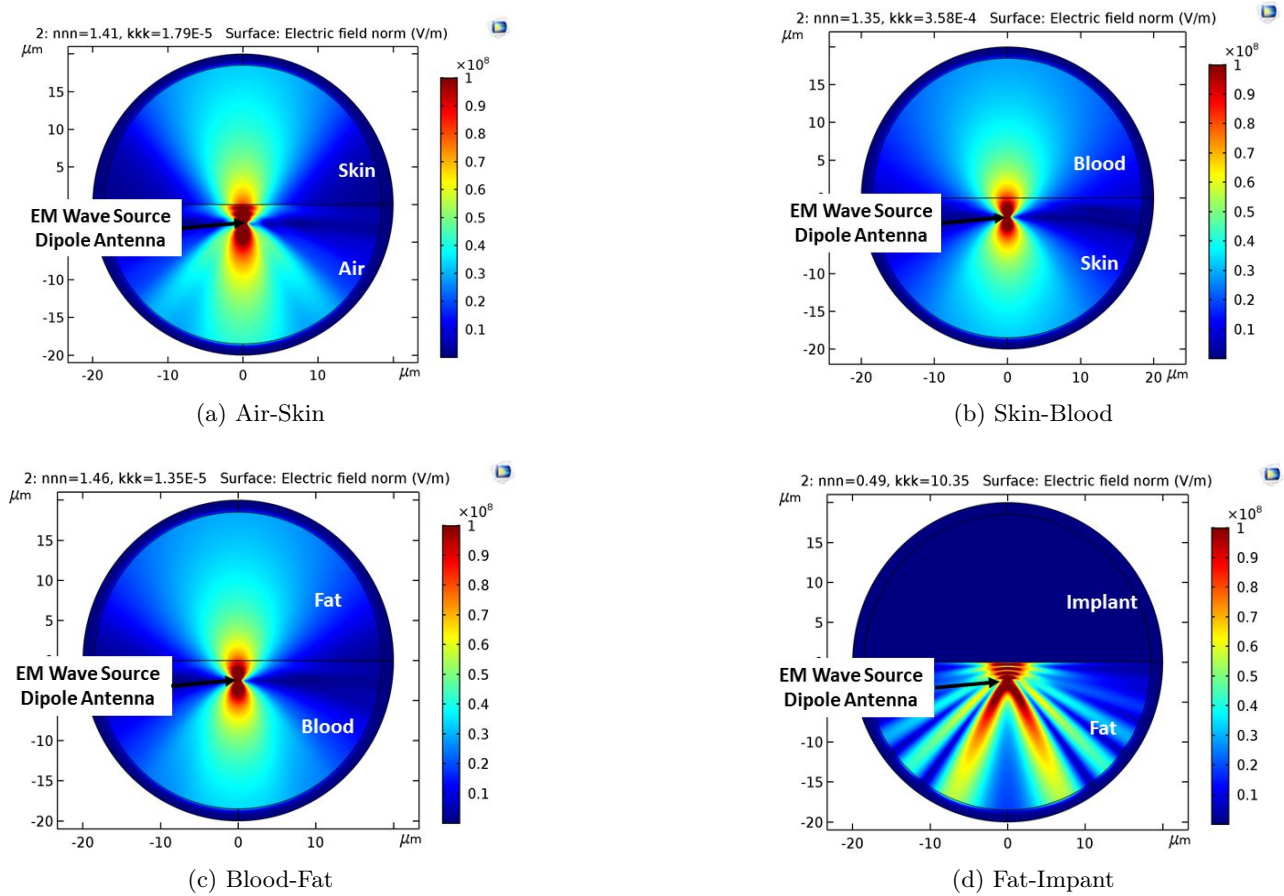


Figure 2: COMSOL Simulations showing the reflection and refraction at the boundary of different layers.

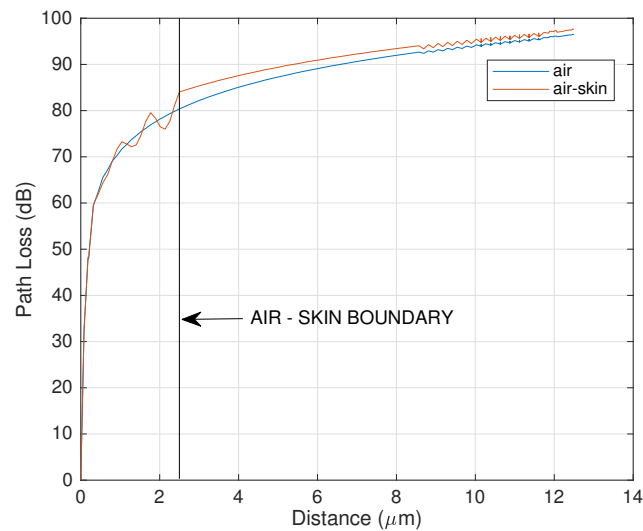


Figure 3: Transition loss at the air-skin boundary.

4.2 Numerical Analysis Results

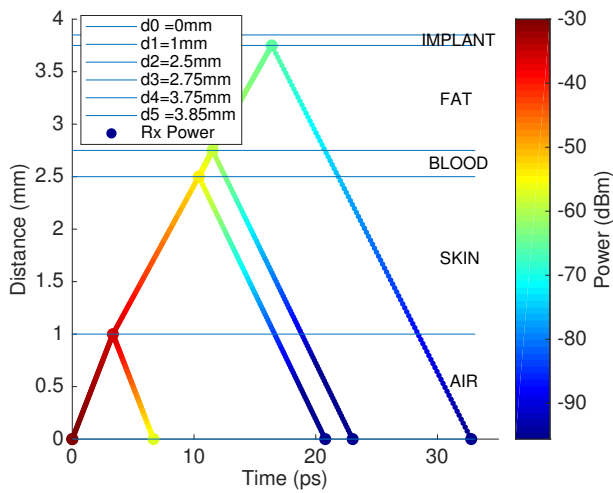
Algorithm 1, summarizes the MATLAB code for numerical link budget analysis given in Section 3 for the proposed model in Figure 1 at Section 2.

Algorithm 1 Algorithm to calculate the power received and reflected at different layers

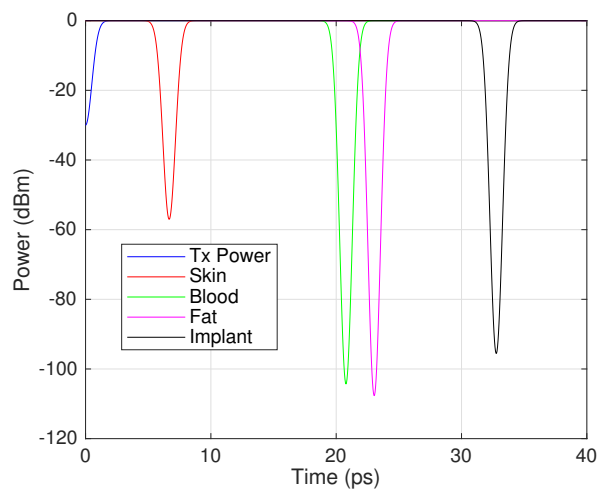
Input: λ , n , d $\triangleright \lambda$: Wavelength, n : Refractive index, d : Thickness of each layer
 μ_{abs}, μ_{red} $\triangleright \mu_{abs}, \mu_{red}$: Absorption and Reduced Scattering Coefficients for each layer
 G_t, G_r, ϕ_{rad} $\triangleright G_t, G_r$: Gains of the Tx and Rx Antennas, ϕ_{rad} : Beam width (in radians)
 θ_{rad}, D, P_t $\triangleright \theta_{rad}$: Beam width (in radians), D : Directivity, P_t : Transmitted power
Output: P_r, P_{ref} $\triangleright P_r$: Power received at each layer, P_{ref} : Power reflected from each layer to laser

1: **for** each layer l **do**
2: $V_l \leftarrow \frac{c}{n_l}$ $\triangleright V_l$: Velocity at layer l ; c : Speed of Light
3: $t_1 \leftarrow 0$
4: $t_l \leftarrow \frac{d_l}{V_{l-1}}$ $\triangleright t_l$: Time to travel layer l
5: $\mu_{as,l} \leftarrow \mu_{abs,l} + \mu_{sca,l}$ $\triangleright \mu_{as,l}$: Absorption and Scattering Coefficient of layer l
6: **end for**
7: **for** each layer l **do**
8: $L_{spr,l} \leftarrow D \times \left(\frac{\lambda_l}{4\pi d_{l+1}}\right)^2$ $\triangleright L_{spr,l}$: Spreading Loss at layer l
9: $L_{as,l} \leftarrow e^{-\mu_{as,l} \times d_{l+1}}$ $\triangleright L_{as,l}$: Absorption and Scattering Loss at layer l
10: $L_{ref,l} \leftarrow R_l = \left(\frac{N_l - N_{l+1}}{N_l + N_{l+1}}\right)^2$ $\triangleright R_l$: Reflectance
11: $L_{bound,l} \leftarrow T_l = 1 - R$ $\triangleright T_l$: Transmittance
12: $Losses_l \leftarrow L_{spr,l} + L_{as,l}$ $\triangleright Losses_l$: Total Path-loss at each layer l
13: **end for**
14: **for** each layer l **do**
15: $P_l \leftarrow P_{r,l-1} + G_t + G_r - |Losses_l|$
16: $P_{r,l} \leftarrow P_l - |L_{bound,l}|$ $\triangleright P_{r,l}$: Power received at layer l
17: $P_{ref,l} \leftarrow P_l - |Losses_1 + \dots + Losses_l| - |L_{ref,l}| - |L_{bound,1} + \dots + L_{bound,l-1}|$ $\triangleright P_{ref,l}$: Power reflected from layer l to laser
18: **end for**
19: **return** P_r, P_{ref}

Figure 4a shows the received power in dBm at different layers of the skin tissue, where the transmitted power from the laser in the wearable device is considered to be 1 μ W (−30 dBm). The implant is considered to be placed within 1 mm of the fat layer (Figure 1). The x axis shows the time that it takes for the light to traverse through the layers and the y axis represents the distance (depth) of the light penetration at different layers of skin. Figure 4b, shows the received signal power at the wearable device after being reflected at each layer boundary. A 500 fs long Gaussian pulse has been considered for the laser transmission as shown in the figure. It can be observed in this figure that the receiver (at the wearable device) receives a weakened copy of the transmitted signal that has been reflected back at from each of the transition boundaries as defined in the multilayer model (Figure 1). It can be observed, that the latest received pulse is the reflected signal from the gold (implant) layer. As it has been shown in simulation results in Figure 2d, due to the high reflectivity of gold, the reflection loss in this boundary is much lower than the other interfaces and hence most of the energy of the signal will be reflected. Therefore, as it can be seen in Figure 4b, there is almost 10 dB difference between the received pulse from implant and the other two closely reflected signals after 20 ps (i.e., from blood and fat layers). Also, note that the first reflected pulse (from the air-skin boundary), although it has a rather high signal strength, but it happens very close (in time) to the transmitted signal. Therefore, the received signal from the implant which includes the desired information, can be distinguished from the other reflection from the cell layer boundaries either with their time difference or their strength.



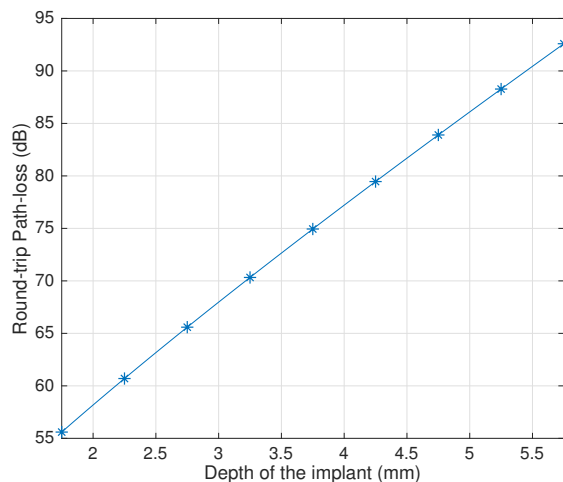
(a) Signal power at different layers of skin tissue



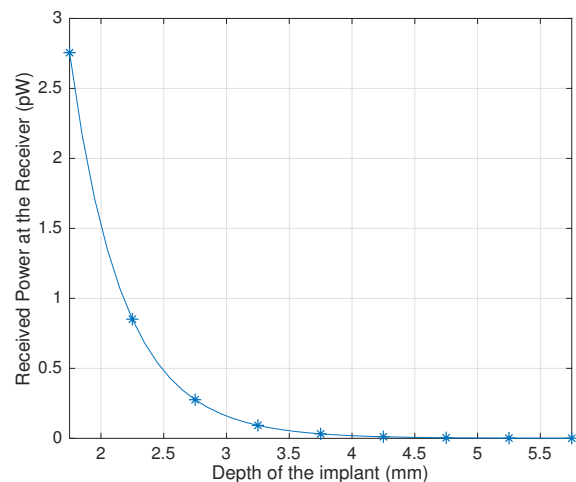
(b) Received power at the receiver from different layers

Figure 4: Power received at different layers of the human tissue @ $P_t = 1\mu W$ and Beam-width of $\theta = 0.5^\circ$, $\phi = 0.5^\circ$. Gaussian pulses represent the signals transmitted and received at the detector after being reflected from each layer boundary of the tissue.

Figure 5a shows the path-loss in dB for the transmitted signal to reach the implant at different depths in mm, and being received back at the wearable device. It can be observed that path-loss linearly increase due to the fact that the impact of the absorption and scattering in the fat layer is dominant loss. Figure 5b shows the received power in pW for a transmitted signal power of $1\mu W$ (-30 dBm) versus different depths of the implant. It can be observed from Figure 5 that for an implant that is placed around 2 mm deep in the skin tissue, the received signal at the receiver experiences almost 60 dB loss, and the received signal exponentially decreases as we go deeper in skin.



(a) Total Path-loss V/S Depth of the Implant



(b) Received Power at Receiver V/S Depth of the Implant

Figure 5: Impact of the depth of the implant with respect to the fat layer thickness ranging from $1\text{mm} - 5\text{mm}$. The total round-trip path-loss and the total received power at the receiver from the implant layer is shown.

Finally, Figure 6 shows the path-loss (6a) and the received signal power (6b) versus the beam width of the transmitted light from the laser in the wearable device. We consider very directional laser with beam widths in the range of $0.5\text{--}5^\circ$ for both $\Delta\theta$, azimuth angle, and $\Delta\phi$, polar angle.¹³ As it can be observed from this figure, the path-loss exponentially increases with wider beam widths. It is related to note, that in all of our numerical analysis we consider a gain of unity for both the transmitter and the receiver antennas. However, both passive and active gains can be considered in the design of the transmitter and receiver antennas by using optical lenses or novel massive antenna array designs respectively. These gains can compensate the very limited transmitting powers of the single micro-ring lasers as well as the very high path-loss of the EM radiation in the skin tissue.

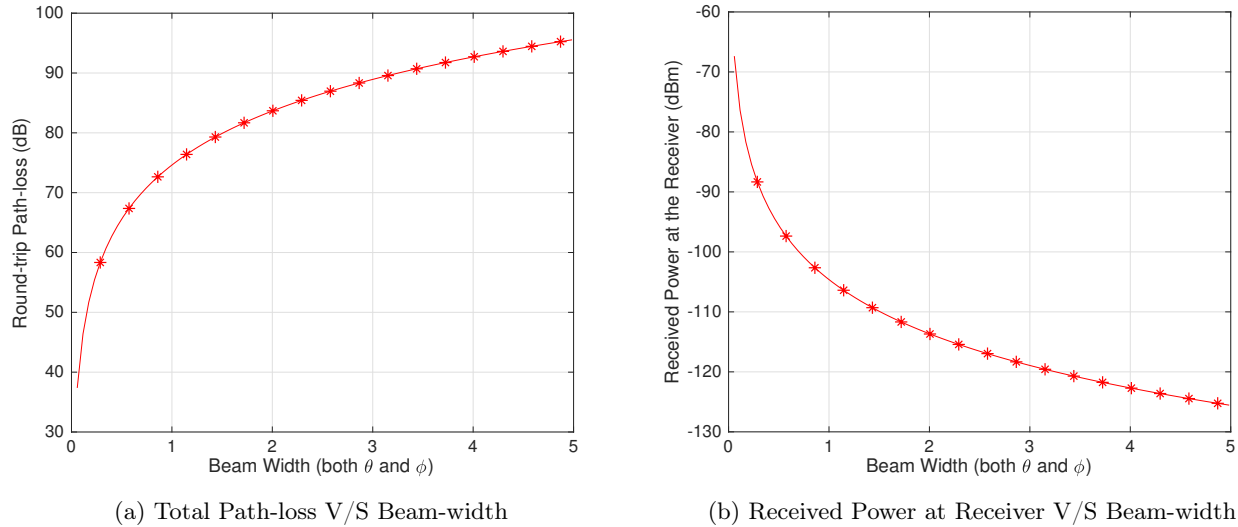


Figure 6: Beam-width of the radiation source ranging as ($\theta = 0.5^\circ - 5^\circ$, $\phi = 0.5^\circ - 5^\circ$). The path-loss and the power received from the implant are shown.

4.3 Link Budget Analysis and Required Sensitivity at the Receiver

The path loss at 1500 nm (200 THz) for a propagating distance of 3.75 mm which comprises of : 1 mm of air region (distance between the wearable device and the skin tissue), 1.5 mm of the skin tissue, 0.25 mm of the blood region and 1 mm of the fat layer (required for the SPR sensor to be in touch with enough amount of blood vessels) can be obtained from Figure 4 and is equal to 65.59 dB. For the transmitter we consider the micro-ring lasers whose peak power density is considered to increase up to 720 MW/cm^2 at wavelength around 1500 nm, and hence have the transmitting power ranging from few hundred nW to few μW .¹³ For our numerical analysis, we use $1 \mu\text{W}$ (-30 dBm) as the power transmitted. Hence, the Received power based on the link budget formula (equation (4)) is:

$$P_R(\text{dBm}) = -30(\text{dBm}) - 65.59(\text{dB}) = -95.59(\text{dBm}), \quad (13)$$

which will be equivalent to 0.31 pW. Considering a SNR of the 10 dB, we have

$$\begin{aligned} \text{SNR} &= P_R - N \\ 10 &= -95.59 - N \end{aligned} \quad (14)$$

The minimum required receiver sensitivity value is -105.59 dBm (0.03 pW). Note that, the state-of-the-art superconducting single-photon detectors are capable to detect powers in the range of tens of pW.¹⁵ Therefore, the received power based on our model is still very low to be detectable. This can be improved by considering high gain antennas (G_R and G_T) both at the receiving and transmitting sides by novel designs such as utilizing massive optical nano-antenna arrays.³³ The power can also be improved by increasing the number of the antenna

elements. Note that the 1 μ W power that is considered in our analysis is the power of only one single micro-ring laser, that can be significantly enhanced by incorporating arrays of nano-antenna elements. In light of these proposed remedies, and by increasing the transmitted power by 30 dB, we can achieve the required signal strength to be detectable at the state-of-the-art superconducting single-photon detectors.¹⁵ This can be done since the laser source (which is the only active part of our proposed architecture) is inside the wearable device that can be equipped with higher power sources and more antenna elements as well as higher gain antennas.

5. CONCLUSION

In this paper, we proposed an architecture to bridge the gap between the commercial wearable devices and the advanced nano-biosensing technologies. More specifically, we thoroughly assessed the feasibility of the wireless optical intercommunications of an SPR-based nanoplasmonic biochip implanted under the wrist, with a nanophotonic wearable smart band which is integrated by an array of nano-lasers and photon-detectors for distributed excitation and measurement of the nanoplasmonic biochip. This is done through a link budget analysis which captures the peculiarities of the intra-body optical channel, the strength of the SPR nanosensor reflection, as well as the capabilities of the nanolasers and the nano photon-detectors. The results show that for an implant which is placed 1 mm under the skin, there is 65.59 dB loss at the received signal reflected from the implant. It is also shown that the directivity of the antenna plays a significant role in the penetration loss as it will exponentially increase the path-loss for wider beam widths. Moreover, there is a trade-off between the depth of the implant to satisfy both the communication and biology requirements to achieve an accurate data collection from the implant to diagnose potential diseases. The proposed analysis guides the development of practical communication designs between the wearable devices and nano-biosensing implants, which paves the way through early-stage diagnosis of severe diseases.

Acknowledgements

This work was supported by the U.S. National Science Foundation (NSF) under Grant No. IIP-1718177.

REFERENCES

- [1] (IDC), I. D. C., “Worldwide quarterly wearable device tracker,” [Online]. Available: <http://www.idc.com/getdoc.jsp?containerId=prUS25903815>, Accessed on: January 2016 .
- [2] Statista, “Use of wearable devices: Which type of wearable device interests you most?,” [Online]. Available: <http://www.statista.com/statistics/259386/us-consumer-interest-in-wearable-computing-devices/>, Accessed on: January 2018 .
- [3] Movassaghi, S., Abolhasan, M., Lipman, J., Smith, D., and Jamalipour, A., “Wireless body area networks: A survey,” *IEEE Communications Surveys & Tutorials* **16**(3), 1658–1686 (2014).
- [4] Eckert, M. A. and Zhao, W., “Opening windows on new biology and disease mechanisms: development of real-time in vivo sensors,” (2013).
- [5] Wong, C. L. and Olivo, M., “Surface plasmon resonance imaging sensors: a review,” *Plasmonics* **9**(4), 809–824 (2014).
- [6] Nguyen, H. H., Park, J., Kang, S., and Kim, M., “Surface plasmon resonance: a versatile technique for biosensor applications,” *Sensors* **15**(5), 10481–10510 (2015).
- [7] Qureshi, A., Gurbuz, Y., and Niazi, J. H., “Biosensors for cardiac biomarkers detection: A review,” *Sensors and Actuators B: Chemical* **171**, 62–76 (2012).
- [8] Yang, M., Yi, X., Wang, J., and Zhou, F., “Electroanalytical and surface plasmon resonance sensors for detection of breast cancer and alzheimer’s disease biomarkers in cells and body fluids,” *Analyst* **139**(8), 1814–1825 (2014).
- [9] Vendrell, M., Maiti, K. K., Dhaliwal, K., and Chang, Y.-T., “Surface-enhanced raman scattering in cancer detection and imaging,” *Trends in biotechnology* **31**(4), 249–257 (2013).
- [10] Hudson, S. D. and Chumanov, G., “Bioanalytical applications of sers (surface-enhanced raman spectroscopy),” *Analytical and bioanalytical chemistry* **394**(3), 679–686 (2009).

- [11] Wu, L. and Qu, X., “Cancer biomarker detection: recent achievements and challenges,” *Chemical Society Reviews* **44**(10), 2963–2997 (2015).
- [12] Aoki, P. H., Furini, L. N., Alessio, P., Aliaga, A. E., and Constantino, C. J., “Surface-enhanced raman scattering (sers) applied to cancer diagnosis and detection of pesticides, explosives, and drugs,” *Reviews in Analytical Chemistry* **32**(1), 55–76 (2013).
- [13] Feng, L., Wong, Z. J., Ma, R.-M., Wang, Y., and Zhang, X., “Single-mode laser by parity-time symmetry breaking,” *Science* **346**(6212), 972–975 (2014).
- [14] Miao, P., Zhang, Z., Sun, J., Walasik, W., Longhi, S., Litchinitser, N. M., and Feng, L., “Orbital angular momentum microlaser,” *Science* **353**(6298), 464–467 (2016).
- [15] Korneev, A., Kouminov, P., Matvienko, V., Chulkova, G., Smirnov, K., Voronov, B., Gol’tsman, G., Currie, M., Lo, W., Wilsher, K., et al., “Sensitivity and gigahertz counting performance of nbn superconducting single-photon detectors,” *Applied Physics Letters* **84**(26), 5338–5340 (2004).
- [16] Johari, P. and Jornet, J. M., “Nanoscale optical wireless channel model for intra-body communications: Geometrical, time, and frequency domain analyses,” *IEEE Transactions on Communications* (2018).
- [17] Guo, H., Johari, P., Jornet, J. M., and Sun, Z., “Intra-body optical channel modeling for in vivo wireless nanosensor networks,” *IEEE transactions on nanobioscience* **15**(1), 41–52 (2016).
- [18] Miccio, L., Memmolo, P., Merola, F., Netti, P., and Ferraro, P., “Red blood cell as an adaptive optofluidic microlens,” *Nature communications* **6** (2015).
- [19] Choi, M., Choi, J. W., Kim, S., Nizamoglu, S., Hahn, S. K., and Yun, S. H., “Light-guiding hydrogels for cell-based sensing and optogenetic synthesis in vivo,” *Nature photonics* **7**(12), 987–994 (2013).
- [20] Elayan, H., Johari, P., Shubair, R. M., and Jornet, J. M., “Photothermal modeling and analysis of intra-body terahertz nanoscale communication,” *IEEE transactions on nanobioscience* (2017).
- [21] Bashkatov, A., Genina, E., Kochubey, V., and Tuchin, V., “Optical properties of human skin, subcutaneous and mucous tissues in the wavelength range from 400 to 2000 nm,” *Journal of Physics D: Applied Physics* **38**(15), 2543 (2005).
- [22] Elayan, H., Shubair, R. M., Jornet, J. M., and Mitra, R., “Multi-layer intrabody terahertz wave propagation model for nanobiosensing applications,” *Nano Communication Networks* **14**, 9–15 (2017).
- [23] Brolo, A. G., Gordon, R., Leathem, B., and Kavanagh, K. L., “Surface plasmon sensor based on the enhanced light transmission through arrays of nanoholes in gold films,” *Langmuir* **20**(12), 4813–4815 (2004).
- [24] Sharpe, J. C., Mitchell, J. S., Lin, L., Sedoglavich, N., and Blaikie, R. J., “Gold nanohole array substrates as immunobiosensors,” *Analytical Chemistry* **80**(6), 2244–2249 (2008).
- [25] Klose, A. D. and Larsen, E. W., “Light transport in biological tissue based on the simplified spherical harmonics equations,” *Journal of Computational Physics* **220**(1), 441–470 (2006).
- [26] Xia, J. and Yao, G., “Angular distribution of diffuse reflectance in biological tissue,” *Applied optics* **46**(26), 6552–6560 (2007).
- [27] Ciddor, P. E., “Refractive index of air: new equations for the visible and near infrared,” *Applied optics* **35**(9), 1566–1573 (1996).
- [28] Vuylsteke, M., Vandekerckhove, P., De Bo, T., Moons, P., and Mordon, S., “Use of a new endovenous laser device: results of the 1,500 nm laser,” *Annals of vascular surgery* **24**(2), 205–211 (2010).
- [29] Maier, J. S., Walker, S. A., Fantini, S., Franceschini, M. A., and Gratton, E., “Possible correlation between blood glucose concentration and the reduced scattering coefficient of tissues in the near infrared,” *Optics letters* **19**(24), 2062–2064 (1994).
- [30] Johnson, P. B. and Christy, R.-W., “Optical constants of the noble metals,” *Physical review B* **6**(12), 4370 (1972).
- [31] Elayan, H., Shubair, R. M., Jornet, J. M., and Johari, P., “Terahertz channel model and link budget analysis for intrabody nanoscale communication,” *IEEE transactions on nanobioscience* **16**(6), 491–503 (2017).
- [32] [COMSOL Multiphysics Simulation Software], COMSOL. [Online]. Available: <http://www.comsol.com/products/multiphysics/>.
- [33] Sangwan, A., Nafari, M., Johari, P., and Jornet, J. M., “Time-delay beamforming for optical nano-antenna arrays,” to appear in *Proc. of the SPIE Defense + Commercial Sensing (DCS), International Society for Optics and Photonics, Orlando, FL* (2018).